Mass-spring model for acoustic metamaterials consisting of a compact linear periodic array of dead-end resonators

Maël LOPEZ,[1,a] Thomas DUPONT,[1] Raymond PANNETON,[2]

[1] *Department of Mechanical Engineering, École de Technologie Supérieure, 1100 rue Notre-Dame Ouest, Montréal, Québec, H3C 1K3, Canada*

[2] *CRASH-UdeS, Department of Mechanical Engineering, Université de Sherbrooke, 2500 boul. de l'Université, Sherbrooke, Québec, J1K 2R1, Canada*

2023/11/22

[a] Mael.Lopez.1@ens.etsmtl.ca

Abstract

This paper presents a mass-spring model to predict the normal incidence acoustic response of a metamaterial composed of a compact linear periodic array of dead-end resonators. The dead-end resonators considered are ring-shaped Helmholtz resonators. The model is based on a mass-spring analogy and considers the thermoviscous losses in the metamaterial following an effective fluid approach. A matrix equation of acoustic motion is derived for the finite case of N-periodic arrays. Under external excitation, its direct solution predicts the sound absorption coefficient and transmission loss. Under the homogeneous case, the solution of its associated eigenvalue problem predicts the acoustic eigenfrequencies and mode shapes. The dispersion relation is also solved to predict the beginning of the first stopband, and a low frequency approximation allows developing a formula to estimate the first eigenfrequency. The results show that the system with N degrees-of-freedom has three stopbands over the frequency range studied, with zero sound absorption and transmission. The model also helps to understand how the acoustic dissipation, at a given resonant frequency, is affected by the position of the acoustic velocity nodes (eigenmodes) in the geometry of the metamaterial. Prototypes are designed, manufactured, and tested in an impedance tube to validate the model.

I. INTRODUCTION

Conventional acoustic materials, such as porous materials and resonators, are sometimes not suitable for noise mitigation at low frequencies. Indeed, at these frequencies, they may require a significant thickness to obtain good acoustic properties (sound absorption and/or sound transmission loss). Research is moving towards new solutions such as subwavelength acoustic metamaterials. When properly engineered, subwavelength acoustic metamaterials have good acoustic properties at small thickness-to-wavelength ratios; generally smaller than 1/10, even 1/100, against 1/5 for conventional materials. Different types of acoustic metamaterials exist such as membrane-type[1], structured resonators[2–4], surface arrangements[4–6] or dead-end periodic structures[7,8]. Dead-end (DE) structures are composed of a main pore with a periodic arrangement of lateral resonators. The periodic arrangement of DE is responsible for the effective increase in air compressibility in the main pore[7]. Due to this increase, the effective celerity is decreased as well as the resonance frequencies of the material. Following this principle, these materials are also known as "slow sound materials"[8].

The first studies of these periodic DE materials focused on straight quarter-wavelength resonators as the DE structures[7–9]. Also, side branch Helmholtz resonators were used as DE resonators[10,11]. In another way, Dupont et al.[12] proposed to use ring-shaped cavities around the main pore as DE resonators. Such a resonator is the equivalent of an axisymmetric quarter-wavelength resonator. It will be called hereafter quarter-wavelength annular resonator. Linear periodic arrangements of these DE resonators were the subject of other studies: Brooke et al.[13] investigated the nonlinear response of these materials at high sound pressure level, while numerical modelling was done to effectively consider thermo-viscous losses in the metamaterial[14].

In this paper, a variant of the ring-shaped quarter-wavelength annular resonator is studied. It is an annular (or ring-shaped) Helmholtz resonator (AHR). It is formed by an annular neck connected to an annular cavity. Therefore, the whole material is composed of a compact linear periodic array of AHR along a main central cylindrical pore. This metamaterial will be called multi-AHR.

To study periodic DE materials, transfer matrix method is commonly used[7,10–12]. However, it does not allow a simple visualization of the phenomena involved, nor to make a detailed analysis of the eigenfrequencies and mode shapes. For this purpose, a mass-spring model, based on a mechanical analogy, is proposed. Mass-spring models are largely used in acoustics to describe Helmholtz resonators with one or more degrees of freedoms[2,15–18]. Periodic mass-spring systems are similar to one-dimensional monatomic harmonic crystals that have been studied for a long time[19]. The aim of this article is to show that previous works on this topic can be transposed to acoustic DE structures with a view to study their propagation behaviors, their dispersion relations, their stopbands, and their natural frequencies and mode shapes. Moreover, a simple formula is derived from the mass-spring analogy to predict the first eigenvalue of the studied metamaterial. Finally, an original mapping of the mass displacement according to the frequencies and the position of the masses is proposed to analyze the complexity of the acoustic phenomena (propagation of the sound, resonances, stopbands and modes) underlying the metamaterial.

The present paper is organized as follows. In Sec. II, the studied geometry is presented. Sec. III presents the model to determine the surface acoustic impedance of an AHR. In Sec. IV, the complete mass-spring model of the metamaterial is presented. It is shown how this model can be transposed to a global transfer matrix. Also, the non-dissipative eigenvalue problem is presented, and a simple expression for the first natural frequency is derived. Sec. V presents the validation of the developed model against experimental impedance tube tests and predictions obtained by another modeling method. Then the sound propagation through the metamaterial is studied. Note that some of the developments presented below were presented in the form of a conference paper[20].

II. MATERIALS

The proposed metamaterial is composed of a compact linear array of periodic unit cell (PUC), see Fig. 1(a). A PUC is composed of a pore ①, a junction ②, and a DE resonator (here an AHR, neck ③ and cavity ④). Fig. 1(b) shows a photo of the manufactured axisymmetric multi-AHR sample. For the experimental part, the samples of the proposed metamaterial is composed of several stackable elements which have been manufactured in aluminum 6061-T6. A 0.45-mm chamfer is present on the contour of the cells to facilitate their assembly and reduce acoustic leaks. The geometry has been designed so that the aluminum plate between cavities ④ is 1-mm thick. Note that the first and last circular pores are shorter than the inner pores. The length of the first and last pores is $l_{end} = 1.5$ mm. The length of the inner pores is $l_p = 2$ mm. The radius of all the pores (viewed as the central main pore) is $r_p = 2$ mm. The neck of an AHR starts at r_p and ends at $r_n = 3$ mm with an annular neck thickness of $h_n = 1$ mm. The AHR cavity ends at radius $r_c = 21$ mm and its thickness is $h_c = 2$ mm. The number of cells is $N = 10$, for a total length of 31 mm. The sample radius is $r_{sample} = 22.22$ mm. The geometric parameters of the sample are summarized in TABLE I.

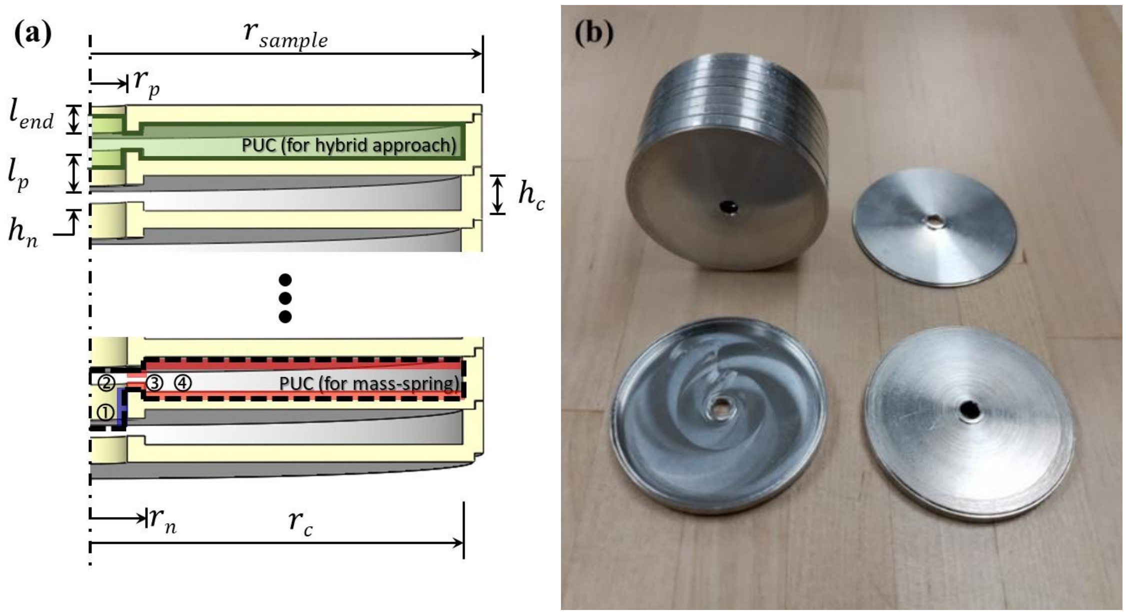

FIG. 1. (color online). (a) Schematic of the axisymmetric sectional view. The dashed black line is the contour of the plane defining the fluid of revolution of the PUC for the mass-spring model of Sec. IV. The bold green line is the contour of the plane defining the fluid of revolution of the PUC for the hybrid approach of Sec. V.A. The thick colored lines are idealized representations of the acoustic boundary layers where thermal and viscous losses appear in the annular Helmholtz resonator (red) and in the main pore (blue). (b) Photo of the manufactured multi-annular Helmholtz resonators sample.

TABLE I. Dimensions of the main parameters of multi-annular Helmholtz resonators sample.

Geometric parameters	l_{end}	l_p	r_p	r_n	h_n	r_c	h_c	r_{sample}
Sample (mm)	1.5	1	2	3	1	21	2	22.22

III. ANNULAR HELMHOLTZ RESONATOR

An AHR is composed of two thin concentric rings aligned and of different thicknesses, identified as ③ and ④ in Fig. 1(b). The subscript n refers to neck and c to cavity. An AHR is supposed to be thin (i.e., small thickness-to-radius ratio h_c/r_c) in a way that only radial propagation is considered. The wave equation for a one-dimensional concentric radial wave is given by[21]

$$\frac{1}{r}\frac{\partial}{\partial r}\left(r\frac{\partial \Psi}{\partial r}\right)-\frac{1}{c^2}\frac{\partial^2 \Psi}{\partial t^2}=0, \tag{1}$$

where r is the radial coordinate, Ψ the acoustic pressure, and c is the sound speed. Each part of the AHR (neck and cavity) is considered as a different media with its own solution of Eq. (1). The air saturating both parts of the AHR has effective fluid properties. These effective properties make it possible to consider the thermal and viscous losses which occur in the acoustic boundary layers along the walls which are perpendicular to the wavefronts in the AHR. As thicknesses h_c and h_n are small, the neck and the cavity are considered as slits. The parameters of the representative slits are given in TABLE II. Also, harmonic regime is assumed, $\Psi(r,t)=p(r)e^{j\omega t}$, with t the time and $j^2=-1$. The acoustic pressure in the neck ($s = n$) and cavity ($s = c$) can be expressed as

$$p_s(r)=A_s\mathrm{J}_0(k_s r)+B_s\mathrm{Y}_0(k_s r), \tag{2}$$

where J_m and Y_m are respectively Bessel functions of the first and second kind of order m, A_s and B_s represent the amplitudes of the diverging and converging pressure waves respectively, k_s is the effective wave number of the air in the neck or cavity determined by the JCA model.

TABLE II. Parameters of the Johnson-Champoux-Allard model for circular pores (main pore) and slits (AHR: neck and cavity). In the table, η is the dynamic viscosity of air, r_p is the radius of the main pore and h_s the thickness of the annular neck ($s = n$) and cavity ($s = c$).

JCA parameter	Units	Circular pore	Slits
Porosity		1	1
Tortuosity		1	1
Viscous characteristic length	m	r_p	h_s
Thermal characteristic length	m	r_p	h_s
Static airflow resistivity	Pa·s/m²	$\frac{8\eta}{{r_p}^2}$	$\frac{12\eta}{{h_s}^2}$

The radial acoustic velocity is obtained using the one-dimensional Euler linearized equation with cylindrical coordinates, $-\frac{\partial p(r,t)}{\partial r} = \rho \frac{\partial v(r,t)}{\partial t}$, and is equal to

$$v_s(r) = -\frac{j}{Z_s}[A_s \mathrm{J}_1(k_s r) + B_s \mathrm{Y}_1(k_s r)]. \tag{3}$$

where Z_s is the effective characteristic impedance of the air in the neck or cavity determined by the JCA model.

All AHR boundary walls are supposed rigid and perfectly reflective. This imposes the acoustic velocity to be zero at $r = r_c$. Applying this boundary condition for the cavity on Eq. (3) gives

$$B_c = -A_c \frac{\mathrm{J}_1(k_c r_c)}{\mathrm{Y}_1(k_c r_c)}. \tag{4}$$

The surface impedance at the entrance of the annular cavity is determined by substituting Eq. (4) into Eqs. (2) and (3) at $r = r_n$. This yields

$$Z_{S,c} = \frac{p_c(r_n)}{v_c(r_n)} = jZ_c \frac{\mathrm{J}_0(k_c r_n) - \frac{\mathrm{J}_1(k_c r_c)}{\mathrm{Y}_1(k_c r_c)}\mathrm{Y}_0(k_c r_n)}{\mathrm{J}_1(k_c r_n) - \frac{\mathrm{J}_1(k_c r_c)}{\mathrm{Y}_1(k_c r_c)}\mathrm{Y}_1(k_c r_n)}. \quad (5)$$

The continuity of pressure and flow at the interface between the annular neck and cavity at $r = r_n$ leads to

$$\frac{p_n(r_n)}{S_n v_n(r_n)} = \frac{Z_{S,c}}{S_c}, \quad (6)$$

where $S_n = 2\pi r_n h_n$ and $S_c = 2\pi r_n h_c$ are the cylindrical surfaces of the annular neck and cavity at r_n. Substituting Eqs. (2) and (3) into Eq. (6) gives

$$jZ_n \frac{A_n \mathrm{J}_0(k_n r_n) + B_n \mathrm{Y}_0(k_n r_n)}{A_n \mathrm{J}_1(k_n r_n) + B_n \mathrm{Y}_1(k_n r_n)} = \frac{h_n}{h_c} Z_{S,c}. \quad (7)$$

By rearranging Eq. (7), the ratio between both amplitudes A_n and B_n can be expressed as

$$\Upsilon = \frac{B_n}{A_n} = \frac{\frac{h_n Z_{S,c}}{h_c\, jZ_n}\mathrm{J}_1(k_n r_n) - \mathrm{J}_0(k_n r_n)}{\mathrm{Y}_0(k_n r_n) - \frac{h_n Z_{S,c}}{h_c\, jZ_n}\mathrm{Y}_1(k_n r_n)}. \quad (8)$$

Now, the surface impedance of an AHR (or at the entrance of the annular neck) is obtained from Eq. (2) and Eq. (3). It is given by

$$Z_{S,AHR} = \frac{p_n(r_p)}{v_n(r_p)} = jZ_n \frac{\mathrm{J}_0(k_n r_p) + \Upsilon \mathrm{Y}_0(k_n r_p)}{\mathrm{J}_1(k_n r_p) + \Upsilon \mathrm{Y}_1(k_n r_p)}. \quad (9)$$

$Z_{S,AHR}$ is the input impedance of an AHR seen by the main pore. Subsequently, this impedance will be used in the mass-spring model described in the next section.

IV. MASS-SPRING MODEL FOR A METAMATERIAL

Previous research has shown that periodic DE metamaterials can be modeled using the lumped parameter model[7,12]. The lumped parameter model is generally used with the transfer matrix formulation which gives good agreement with experimental results. However, the transfer matrix method does not allow to give a simple interpretation of the acoustical behavior of a metamaterial, nor to extract analytic formulas of its natural frequencies. For this purpose, the lumped parameter model is employed following a mass-spring analogy. A mass-spring representation of the PUC shown in Fig.1(b) is depicted in Fig. 2.

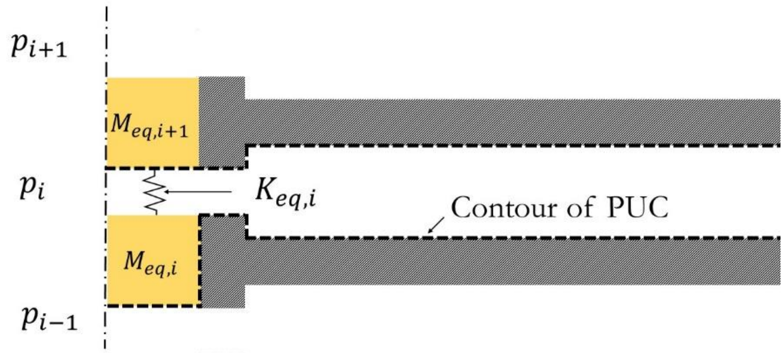

FIG. 2. (color online). Mass-spring representation at junction i of the PUC shown in Fig. 1(b).

A. Mass-spring model

1. The lumped model

In a mass-spring analogy, each pore is represented by a corresponding equivalent mass. That is verified if the effective wavelength of a pore is much smaller than its length. To consider viscous losses, the air density is replaced by an effective density of the corresponding pore. The effective density is given by the JCA model for a cylindrical pore with the parameters given in TABLE II. Note that the term "equivalent" refers to a lumped property of the mass-spring system (mass for a pore, stiffness for a cavity), while the term "effective" refers to the properties of the air saturating a component of the metamaterial (i.e.: pore, neck, or cavity). The equivalent mass of the ith pore is

$$M_{eq,i} = \rho_p A_p l_i, \tag{10}$$

where ρ_p is the effective density of the air in the pore, $A_p = \pi r_p^2$ is the pore cross-sectional area, $l_i = l'_p$ for $2 \leq i \leq N$, and $l_i = l'_{end}$ for $i = 1$ and $i = N + 1$. It is worth mentioning that l'_p, respectively l'_{end}, is the corrected length to account for radiation effect on both sides of each inner pore, respectively end pore. From the inner side, an end pore radiates into an AHR cavity, and from the other side it radiates into the exterior medium. For the exterior medium radiation, the length correction is calculated by the method proposed by Karal[22], l_{Karal}. For the inner side, where a pore radiates into an AHR, the geometry studied is outside the limits of the formulas of length correction given by Karal[22] and Ingard[23]. In fact, their formulas predict a length correction greater than the distance h_n between two consecutive pores. With this observation, an intuitive and logical approach is that the maximum end correction should not exceed half the distance between two pores. Thus, the author proposes to use the corrected length $l'_p = l_p + h_n$ for the inner pores and $l'_{end} = l_{end} + l_{Karal} + \frac{h_n}{2}$ for the exterior pores. For the geometry described in the previous section and inserted in an impedance tube of the same radius r_{sample} as the metamaterial sample, $l'_p = 3.0$ mm and $l'_{end} = 3.5$ mm.

Applying Newton's second law on the first pore, $i = 1$, the equation of motion is

$$M_{eq,1}\frac{\partial^2 x_1}{\partial t^2} = -p_1 A_p + A_p P_1, \tag{11}$$

where x_1 is the acoustic displacement relative to the first mass, p_1 is the acoustic pressure at the first junction (identified as ② in Fig. 1(b)), and P_1 is the total acoustic pressure at the input of the metamaterial. Similarly, applying Newton's second law on the inner pores, $2 \le i \le N$, the equation of motion is

$$M_{eq,i}\frac{\partial^2 x_i}{\partial t^2} = -p_i A_p + p_{i-1} A_p, \tag{12}$$

where x_i is the acoustic displacement of mass i, p_i and p_{i-1} the acoustic pressures at junctions i and $i-1$. Finally, applying Newton's second law on the last pore, $i = N+1$, the equation of motion is

$$M_{eq,N+1}\frac{\partial^2 x_{N+1}}{\partial t^2} = p_N A_p - A_p P_{N+1}, \tag{13}$$

where P_{N+1} is the total acoustic pressure at the exit of the metamaterial.

To solve the equations of motion, the pressures before and after a junction need to be determined. Inside the junction, the pressure is assumed to be constant, and the losses are negligible compared to that of the cavities and pores. The pressure at any junction i can be written as[24]

$$p_i = -\rho_0 c_0^2 \frac{\Delta V_J}{V_J}, \tag{14}$$

where ρ_0 and c_0 are the adiabatic density and sound speed of the air in the junction, ΔV_J is the variation of the junction volume, and $V_J = A_p h_n$ is the junction volume. The variation of volume at junction i can be expressed as

$$\Delta V_J = -x_i A_p + \xi_{de,i} A_{de} + x_{i+1} A_p\ , \tag{15}$$

where x_i and x_{i+1} are the acoustic displacements relative to the upstream and downstream masses connected to junction i, $\xi_{de,i}$ is the radial acoustic displacement at the input of the DE resonator, and $A_{de} = 2\pi r_p h_n$ is the common area between the junction and the DE.

Using harmonic dependence, the relation between the acoustic radial velocity and displacement is $v_{de} = j\omega\xi_{de}$. Assuming continuity of pressure at the interface between the junction and the neck of the AHR, the surface impedance at the input of the ith AHR is given by $Z_{S,AHR} = p_i / v_{de,i}$ (all AHRs are identical in the metamaterial). Substituting this result into Eq. (15) and substituting Eq. (15) into Eq. (14) gives the pressure at junction i:

$$p_i = \frac{x_i - x_{i+1}}{\frac{V_J}{\rho_0 c_0^2} + \frac{A_{de}}{j\omega Z_{S,AHR}}} A_p \quad \forall\, i = 1, 2, \dots N. \tag{16}$$

Therefore, the value of p_{i-1} is deduced. It is given by

$$p_{i-1} = \frac{x_{i-1} - x_i}{\frac{V_J}{\rho_0 c_0^2} + \frac{A_{de}}{j\omega Z_{S,AHR}}} A_p \quad \forall\ \ i = 2, \dots N+1. \tag{17}$$

Using Eq. (16) and Eq. (17), Eqs. (11), (12) and (13) can be rewritten in a matrix form

$$\left(-\omega^2 \mathbf{M_{eq}} + \mathbf{K_{eq}}\right)\mathbf{x} = \mathbf{f}. \tag{18}$$

where $\mathbf{x} = \{x_1\ x_2\ \dots\ x_{N+1}\}^t$ is the acoustic displacement vector relative to the masses, $\mathbf{f} = \left\{A_p P_1\ 0\ \dots\ 0\ -A_p P_{N+1}\right\}^t$ is the force vector, and superscript t refers to the transposed vector. The equivalent mass matrix, $\mathbf{M_{eq}}$, is diagonal and is written as

$$\mathbf{M_{eq}} = \begin{bmatrix} M_{eq,1} & & & & 0 \\ & M_{eq,2} & & & \\ & & \ddots & & \\ & & & M_{eq,N} & \\ 0 & & & & M_{eq,N+1} \end{bmatrix}. \tag{19}$$

The equivalent spring matrix, $\mathbf{K_{eq}}$, is tridiagonal and is written as

$$\mathbf{K}_{eq} = K_{eq} \begin{bmatrix} 1 & -1 & & & 0 \\ -1 & 2 & -1 & & \\ & & \ddots & & \\ & & -1 & 2 & -1 \\ 0 & & & -1 & 1 \end{bmatrix}, \tag{20}$$

where K_{eq} is the stiffness of the junction coupled with the AHR given by

$$K_{eq} = \frac{A_p^2}{\frac{V_J}{\rho_0 c_0^2} + \frac{A_{de}}{j\omega Z_{S,AHR}}}. \tag{21}$$

Eq. (18) is the matrix equation of acoustic motion which relates the acoustic displacements to the external acoustic forces applied to the metamaterial. It can be rewritten in a more compact form as

$$\mathbf{Ax} = \mathbf{f}, \tag{22}$$

where $\mathbf{A}$ is the dynamic stiffness matrix, a combination of the frequency-dependent mass and stiffness matrices of size $N + 1$.

2. Acoustic indicators and global transfer matrix

For a given force, the displacement of the masses can be deduced from Eq. (22). The normal incidence acoustic impedance at the surface of the sample is given by the ratio of the acoustic pressure and velocity. For the harmonic regime under consideration, it is given by $Z_s = P_1 / j\phi\omega x_1$, with $\phi = A_p / A_{sample}$ and $A_{sample} = \pi r_{sample}^2$, the cross-section area of the sample. Note here that the metamaterial sample is inserted into a tube of the same diameter (configuration similar to an impedance tube test). From Z_s, the normal incidence reflection coefficient R, incident pressure P_i, and sound absorption coefficient α can be deduced, respectively, from: $R = (Z_s - \rho_0 c_0)/(Z_s + \rho_0 c_0)$, $P_i = P_1/(1+R)$, and $\alpha = 1 - |R|^2$. If the sample is backed by a rigid and perfectly reflective wall, x_{N+1} must be imposed to zero prior to solving Eq. (22). If the sample is backed by an anechoic termination, the impedance at the rear surface is equal to the characteristic impedance of the transmission fluid, that is $\rho_0 c_0$. Then the surface impedance at the rear surface of the sample is $P_{N+1}/j\phi\omega x_{N+1} = \rho_0 c_0$. By continuity, the transmitted pressure is $P_t = P_{N+1} = j\omega\phi\rho_0 c_0 x_{N+1}$, and the normal incidence sound transmission loss is $TL = -10\log\,(P_t/P_i)$.

Another way to compute the acoustic response of the metamaterial is by converting Eq. (22) into a transfer matrix. Eq. (22) can be modified to link the acoustic pressure and velocity as

$$\mathbf{Zu} = \mathbf{p}, \tag{23}$$

where $\mathbf{Z} = \mathbf{A}/j\omega A_p$ is the acoustic impedance matrix, $\mathbf{u} = \partial\mathbf{x}/\partial t = j\omega\mathbf{x}$ is the acoustic velocity vector, and $\mathbf{p} = \{P_1\ 0\ \dots\ 0\ P_{N+1}\}^t$ is the acoustic pressure vector. Second, Eq. (23) is rewritten in a four-pole transfer pressure-velocity matrix formulation. The transfer matrix $\mathbf{T_M}$ of the metamaterial links the upstream acoustic fields to the downstream acoustic fields by the following relation:

$$\begin{pmatrix} p_1 \\ u_1 \end{pmatrix} = \mathbf{T_M} \begin{pmatrix} p_{N+1} \\ u_{N+1} \end{pmatrix}, \tag{24}$$

where p_1 and u_1 correspond to the acoustic pressure and velocity at the input pore of the metamaterial, respectively, p_{N+1} and u_{N+1} correspond to the acoustic pressure and velocity at the output pore of the metamaterial. The demonstration of the transition between the two formulations is presented in the Appendix. The transfer matrix of the metamaterial can be written as

$$\mathbf{T}_{\mathrm{M}} = (-1)^{N+1} \begin{bmatrix} \dfrac{\det(\mathbf{Z}_{1:N,1:N})}{\det(\mathbf{Z}_{2:N+1,1:N})} & \dfrac{\det(\mathbf{Z})}{\det(\mathbf{Z}_{2:N+1,1:N})} \\ -\dfrac{\det(\mathbf{Z}_{1:N,2:N+1})}{\det(\mathbf{Z})} + \dfrac{\det(\mathbf{Z}_{1:N,1:N})\det(\mathbf{Z}_{2:N+1,2:N+1})}{\det(Z)\det(\mathbf{Z}_{2:N+1,1:N})} & \dfrac{\det(\mathbf{Z}_{2:N+1,2:N+1})}{\det(\mathbf{Z}_{2:N+1,1:N})} \end{bmatrix}, \quad (25)$$

where the subscripts on $\mathbf{Z}$ represent submatrix (rows and columns) of $\mathbf{Z}$, and $\det$ refers to the matrix determinant.

Since the two end pores of the metamaterial open to an outside air medium, the global matrix of the metamaterial sample $\mathbf{T}_G$ is obtained by multiplying $\mathbf{T}_M$ by section change transfer matrices

$$\mathbf{T}_G = \mathbf{T}_\phi \, \mathbf{T}_M \, \mathbf{T}_\phi^{-1}, \quad (26)$$

where

$$\mathbf{T}_\phi = \begin{bmatrix} 1 & 0 \\ 0 & \phi \end{bmatrix}, \quad (27)$$

with ϕ as defined previously. Here, it is assumed that upstream and downstream exterior air media are identical and of the same lateral dimensions as the metamaterial sample.

The normal incidence sound transmission loss (anechoic-backed) and the sound absorption coefficient (hard-backed) of the metamaterial sample can be deduced from the global transfer matrix. They are respectively given by

$$TL = 20\log_{10}\left|\frac{T_{G,11} + T_{G,12}/\rho_0 c_0 + T_{G,21}\rho_0 c_0 + T_{G,22}}{2}\right| \text{ (anechoic-backed)} \quad (28)$$

and

$$\alpha = 1 - \left|\frac{T_{G,11} - T_{G,21}\rho_0 c_0}{T_{G,11} + T_{G,21}\rho_0 c_0}\right|^2 \text{ (hard-backed).} \quad (29)$$

with $T_{G,ab}$ the elements of the global transfer matrix, where a and b refer to the row and column of $\mathbf{T}_G$.

B. Dispersion relation

To determine a simple expression for the dispersion relation of our system, we consider this one as a perfect periodic structure. In this case, all the masses in the mass-spring system are identical and given by $M_{eq} = \rho_p A_p h_p$, and the stiffness is given by Eq. (21). The structure is similar to a one-dimensional monatomic chain and the dispersion relation is given by[25]

$$\omega^2 = 4\frac{K_{eq}}{M_{eq}}\sin^2\left(\frac{q h_{cell}}{2}\right), \tag{30}$$

where q is the wave number and h_{cell} the cell thickness $h_{cell} = l'_p + h_n$.

C. Natural frequencies – lossless case

One of the interests of the mass-spring analogy is that the natural frequencies and mode shapes can be determined by solving the eigenvalue problem. One of the goals is to predict frequencies at which absorption peaks occur for the hard-backed termination. In this way, displacement of the last mass is imposed to zero, that is $x_{N+1} = 0$.

1. Eigenvalue problem

Since the last mass displacement is zero, the last row and column of the dynamic stiffness matrix $\mathbf{A}$ are eliminated. Previously, the losses were considered in the mass and stiffness matrices. For the estimation of the natural frequencies, the lossless case is considered. All the effective properties are replaced by adiabatic air fluid properties, c_0 and ρ_0, in the calculations of the equivalent mass, Eq. (10), and stiffness, Eq. (21). In this case, the equivalent mass and stiffness will be identified by $M^0_{eq,i}$ and K^0_{eq}. While $M^0_{eq,i}$ is now real-valued and independent of frequency, K^0_{eq} is real but still depends on frequency due to the Bessel functions. The eigenvalues (natural frequencies) are obtained by solving numerically

$$\det\left(\mathbf{A}^0_{1:N,1:N}\right) = 0. \tag{31}$$

where $\mathbf{A}^0_{1:N,1:N}$ is the lossless dynamic stiffness matrix for the hard-backed termination.

2. Expression of the first natural frequency

To obtain a simple formula of the first natural frequency, perfect periodic structure, lossless and low frequency assumptions need to be made. First, the metamaterial is assumed to be perfectly periodic, that is to say that all the equivalent masses are identical (the first mass end correction due to exterior medium radiation are not considered). In this case the wave number for the hard-backed termination can be rewritten as[25] $qh_{cell} = \frac{2n-1}{2N+1}\pi$, and all equivalent masses are identical, i.e. $M_{eq,i} \rightarrow M_{eq}$. Substituting this wavenumber into Eq. (30) gives the eigen angular frequencies in the perfectly periodic case

$$\omega_n = 2\sqrt{\frac{K_{eq}}{M_{eq}}}\sin\left(\frac{2n-1}{2N+1}\frac{\pi}{2}\right). \tag{32}$$

where n is for the nth eigenvalue.

Now, neglecting the thermoviscous losses, M_{eq}^0 and K_{eq}^0 can be substituted for M_{eq} and K_{eq} in Eq. (32). Note that $M_{eq}^0 = \rho_0 A_p l_p'$ is real-valued and constant. For its part, the stiffness can be simplified further under the assumption of low frequency development when $kr_c \ll 1$ and $kr_n \ll 1$. The first order Taylor series of Bessel functions for small arguments are[26] $\mathrm{J}_0(z) \approx 1$, $\mathrm{Y}_0 \approx 2/\pi \ln z$, $\mathrm{J}_1(z) \approx z/2$ and $\mathrm{Y}_1(z) \approx -(z\pi/2)^{-1}$. With this low frequency assumption, the AHR surface impedance, Eq. (9), simplifies to

$$Z_{S,AHR} \approx 2j\rho_0 c_0^2\left[\omega r_p\left(1 - \frac{r_n^2}{r_p^2} + \frac{h_c}{h_n}\frac{r_c^2}{r_p^2}\left(1 - \frac{r_c^2}{r_n^2}\right)\right)\right]^{-1}. \tag{33}$$

For multi-AHR, perfectly periodic and without thermoviscous losses, Eq. (33) allows the following simplification

$$\sqrt{\frac{K_{eq}}{M_{eq}}} \approx c_0\sqrt{\frac{A_p}{l_p'(V_{de}+V_J)}}, \tag{34}$$

where $V_{de} = \pi r_c^2 h_c - \pi r_n^2(h_c - h_n) - V_J$ is the volume of an AHR, and $V_J = \pi r_p^2 h_n$. Considering the first natural frequency and enough cell repetitions ($N = 10$ in this study), the sine function of Eq. (32) is approximated by its first order Taylor series $\sin(z) \approx z$. For hard-backed termination, the first natural frequency of a multi-AHR can be approximated by

$$f_1 \approx \frac{c_0}{2(2N+1)}\sqrt{\frac{A_p}{l'_p(V_{de}+V_J)}}. \tag{35}$$

V. VALIDATION

To validate the previous developments and highlight certain characteristics, normal incidence sound absorption coefficient and sound transmission loss predicted with the mass-spring model on the multi-AHR described above will be compared with two other approaches: hybrid numerical-analytical approach and experimental approach. Before proceeding to the validation, these approaches are briefly detailed.

A. Hybrid numerical-analytical approach

The hybrid numerical-analytical approach is a combination of the finite element method (FEM) and the transfer matrix method (TMM). Its main interest is to explicitly calculate the thermoviscous losses in the acoustic boundary layers, while maintaining a reasonable computing time. This hybrid approach was presented by Kone et al.[14] for multi-quarter-wavelength annular resonators. Here it is used to study the multi-AHR described above.

Firstly, the FEM is used to solve the thermoviscous-acoustic (TVA)[27] problem on a single periodic unit cell of the multi-AHR to extract its four-pole transfer matrix $\mathbf{T}_{\mathrm{PUC}}$, see Fig. 1(b). The cell is axisymmetric and is composed of half a pore, a junction with a side-branch AHR, and half a pore. Rigid wall condition is assumed on all material contours. Secondly, the PUC is periodized N times with the TMM by $(\mathbf{T}_{\mathrm{PUC}})^N$. On the schematic of Fig.1(b), one notes that it is necessary to add an extra length to the pores at both extremities of the previously periodized structure. This operation is necessary to take into account the fact that $\frac{l_p}{2} < l_{end}$ in the fabricated sample, and the additional length due to the radiation effect in the exterior medium. The transfer matrix of each of these extra pore lengths is obtained analytically by

$$\mathbf{T}_{end} = \begin{bmatrix} \cos{(k_p\delta')} & jZ_p\sin{(k_p\delta')} \\ \frac{j}{Z_p}\sin{(k_p\delta')} & \cos{(k_p\delta')} \end{bmatrix}, \tag{36}$$

with $\delta = l_p - (h_c - h_n)$ and the corrected associated length is δ'. This length is calculated according to the Karal[22] method. For the studied geometry, $\delta' = 2.0$ mm.[28] Thirdly, as for Eq. (26), since the two end pores of the metamaterial open to an outside air medium, the section change transfer matrix of Eq. (27) is used. Consequently, the global matrix of the metamaterial sample for the hybrid approach is given by

$$\mathbf{T}_H = \mathbf{T}_\phi\, \mathbf{T}_{end}\, (\mathbf{T}_{\mathrm{PUC}})^N\, \mathbf{T}_{\mathrm{end}} \mathbf{T}_\phi^{-1}. \tag{37}$$

This equation is finally used to compute the normal incidence sound transmission loss (anechoic-backed) and absorption coefficient (hard-backed) with Eqs. (28) and (29).

In our application of the hybrid approach, the TVA problem was solved with COMSOL Multiphysics 6.0. After validating the FEM model, the CPU time required to solve one converged TVA problem on the studied PUC, at 1500 frequencies from 1 Hz 3000 Hz, was 30 min on a personal computer.

B. Experimental approach: impedance tube

The transmission loss can experimentally be deduced from Eq. (28), where transfer matrix $\mathbf{T}_\mathrm{G}$ is replaced by the measured four-pole transfer matrix. Mecanum impedance tube is used according to the two-cavity three-microphone method[29]. The third microphone is baffled in the center of the rigid moving end (piston) of the tube.

Sound absorption coefficient (hard-backed) can also be deduced from the measured four-pole transfer matrix and Eq. (29). However, due to the high noise attenuation of the metamaterial, the sound absorption coefficient defined by the measured transfer matrix was very noisy. It was preferred to measure directly the sound absorption coefficient (hard-backed) from the two-microphone impedance tube detailed in standard[30]. In this configuration, the sample is backed by a hard termination.

The diameter of the tube is 44.44 mm and the outside diameter of the tested multi-AHR sample of Fig. 1(a) was manufactured to fit in the tube (both diameters are equals). Petroleum jelly is used around the sample to prevent acoustic leakage. The acoustic excitation is random noise between 115 and 4325 Hz is used as acoustic excitation. Each measurement on a sample is repeated five times. Each time, the internal parts are disassembled and then reassembled randomly. Only the two end sections of length l_{end} are kept at extremities. The experimental result presented in the following comparison is the envelope of all these measurements.

C. Comparison of the methods

Firstly, the prediction obtained with the developed mass-spring model on the studied multi-AHR is compared with experimental results and the hybrid approach prediction. The comparison is in terms of the normal incidence sound absorption coefficient for the hard-backed termination, and the normal incidence sound transmission loss for the anechoic-backed termination.

The results are shown in Fig. 3. The results show a good agreement between the three approaches. For the hybrid approach, the added inertial effect, due to the radiation of an internal pore towards its upstream and downstream AHR cavities, is explicitly taken into account by the numerical calculations of the TVA problem on a PUC. It can be noticed that by substituting the corrected length for the internal pores in the mass-spring model, as presented in Sec. A.1, the model predicts a sound absorption coefficient similar to the other two approaches. In Fig. 3, it can be noted that the predictions deviate slightly from each other when the frequency increases. On the one hand, the authors believe that these deviations are due to geometric imperfections of the samples impacting the measurements. Small imperfections are more sensitive as the wavelength is reduced. On the other hand, the thermoviscous losses in the mass-spring model are approximated with the JCA model with parameters for simple canonical pore shapes (cylindrical and slits). While these geometries are, at first order, good idealization of the different parts of the multi-AHR, the real geometries are more complex. Despite these differences, the prediction made with the mass-spring model is rather satisfactory and, a priori, validates the model and the proposed correction for the effective length of the internal pores.

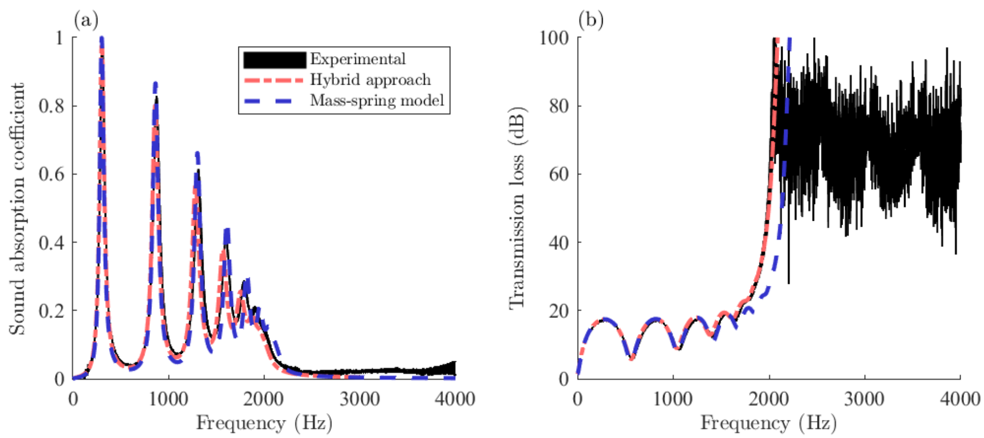

FIG. 3. (Color online). The normal incidence sound absorption coefficient (hard-backed) and transmission loss (anechoic-backed) of the multi-annular Helmholtz resonators sample. Comparison between experimental approach, hybrid approach, and mass-spring model.

In the case of hard-backed termination (absorption problem), Fig. 3(a), the metamaterial presents several peaks of absorption. Absorption peaks are associated with the quarter-wavelength resonances of the metamaterial backed by a rigid termination. This is similar to conventional porous materials. Their position in frequencies depends on the thickness of the metamaterial and its effective properties. For the metamaterial studied, the periodic resonators have the effect of reducing the effective compressibility of the air in the metamaterial (or more precisely that of the air in its central perforation) without modifying its effective density[7,12]. Thus, the effective celerity is reduced and the quarter-wavelength resonances of the metamaterial are shifted towards low frequencies.

In the case of anechoic-backed termination (transmission problem), several lobes of transmission loss spaced by troughs are observed, Fig. 3(b). The troughs of the transmission loss are associated with the half-wave resonances of the metamaterial similar to what occurs in conventional porous materials. And the lobes of transmission loss occur at the anti-resonances, quarter-wave profile, of the metamaterial. However, contrary to conventional materials, the metamaterial shows a stopband starting around 2200 Hz where sound cannot propagate inside the metamaterial. The metamaterial becomes almost purely reflective (the absorption tends to zero and the transmission loss increases). Based on the mass-spring model, Sec. VI.B. discusses in more detail the complexities of acoustic phenomena in relations to the acoustic resonances of the metamaterial and of its resonators in an extended frequency range.

From the previous results, we now focus on the hard backed-termination configuration and absorption peaks. One of the motivations of periodic DE type metamaterials is to have absorption peaks at the lowest possible frequencies and for the lowest total thickness without increasing the volume. Therefore, it is proposed to compare the natural frequencies derived from the mass-spring model, in Sec IV.C, with the resonant frequencies observed on the absorption curves.

The first three rows of TABLE III present the first four resonant frequencies observed on the absorption curves obtained by experiments, hybrid approach and the corrected mass-spring model. Also, TABLE III presents the natural frequencies obtained by the solution of the eigenvalue problem with the lossless assumption, Eq. (31), the lossless and perfectly periodic assumptions, Eq. (32), and the lossless, perfectly periodic, and low frequency assumptions, Eq. (32) with Eq. (34). For the former two, since the equivalent stiffness in Eqs. (31) and (32) is frequency dependent, their solutions are obtained numerically. For the last case, Eq. (32) is solved analytically thanks to Eq. (34). Finally, the last row of the table gives the approximation of the first natural frequency obtained by Eq. (35).

TABLE III shows that for each peak, the resonant frequencies predicted by the three approaches are very close to each other. They diverge by no more than 2.4%. Thus, the resonances predicted by the corrected mass-spring model are, a priori, quite satisfactory. These resonances are now used as a reference to validate the different calculations of the natural frequencies.

In TABLE III, it can be noted that the numerical solution of the eigenvalue problem, Eq. (31), with the lossless approximation, gives eigenfrequencies slightly higher than the resonant frequencies. The relative errors (values in parentheses) are larger at low frequencies and smaller as the frequency increases. This is logical since the viscous and thermal skin thicknesses decrease with frequency and the losses are lower. When the perfectly periodic assumption is added (fifth row of the table), only a slight increase of 1 or 2 % is observed compared to the previous situation. This was expected since the difference between the fabricated sample and the perfectly periodic case is small. In fact, the fabricated sample is the periodic sample with additional thickness (additional pore length of 0.5 mm) at both ends. Consequently, the periodic case has a little less mass at its ends, thus increasing the natural frequencies. Now, if the low frequency approximation is added (Eq. (34)), the first natural frequency (sixth row of the table) deviates only by 1 % from the previous situation. However, the deviation largely increases for higher modes (the low frequency approximation is less appropriate as the frequency increases).

TABLE III. Resonant and natural frequencies for the multi-annular Helmholtz resonators sample described in Sec. II. Comparison between the resonant frequencies obtained by the experimental, hybrid and mass-spring approaches, and the natural frequencies obtained by different approximations derived from the mass-spring model. Values in parentheses are relative errors compared to Mass-spring model.

Resonant/natural frequencies (Hz)	Mode 1	Mode 2	Mode 3	Mode 4
Experimental approach	306	873	1309	1598
Hybrid approach	301	861	1283	1567
Mass-spring model	301	863	1301	1610
Lossless approximation, Eq. (31)	314 (4 %)	887 (3 %)	1333 (2 %)	1646 (2 %)
Lossless and periodic approximation, Eq. (32)	319 (6 %)	899 (4 %)	1345 (3 %)	1656 (3 %)
Lossless, periodic, and low frequency approximations, Eqs. (32) and (34)	322 (7 %)	958 (11 %)	1572 (21 %)	2152 (34 %)
Formula for first natural frequency, Eq. (36)	322 (7 %)	-	-	-

A last estimate is given for the first resonance frequency by Eq. (35) assuming lossless, low frequency and perfect periodic system, with linearization of the sine function. This simple formula gives a relatively good approximation of the first resonant. From this formula, it could be noticed that for minimizing the metamaterial first resonant frequency, the volume of the DE, the pore length or number of cells can be increased. On the contrary, the first resonant frequency increases with the pore cross section area.

VI. DISCUSSION

A. Band structure – dispersion curve

Eq. (30) gives the dispersion relation of an infinite periodic one-dimensional monatomic chain, without low frequency approximation. The dispersion curve, or band structure, with or without losses is shown in Fig. 4(a). It should be mentioned that the results presented in Fig. 4 assume that only plane waves propagate upstream, downstream and in the main pore of the axisymmetric metamaterial. In reality, transverse modes could begin to appear from a cutoff frequency above 30 kHz. The results here aim only to study and understand the fundamental behavior of these metamaterials.

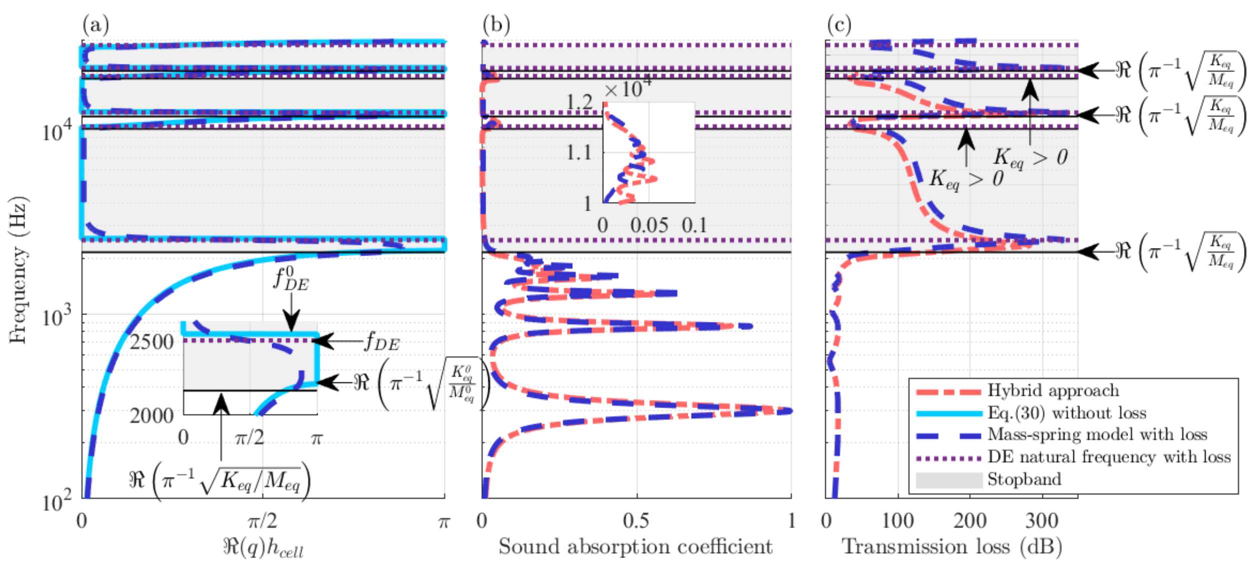

FIG. 4 (Color online). (a) Dispersion curves obtained by Eq. (30), (b) normal incidence sound absorption coefficient (hard-backed), and (c) normal incidence sound transmission loss (anechoic-backed) for the multi-annular Helmholtz resonators. Stopbands are indicated by grey areas and are delineated by black lines.

Unlike conventional mono-atomic chain, the dispersion curve shows alternating passband and stopband before the cutoff frequency (30 kHz). This is due to the frequency dependence of the stiffness. A stopband appears when no energy is carried by the propagating wave, which is equivalent to the real part of the group velocity being zero[31]. So, a stopband starts each time the real part of the nondimensional wavenumber reaches π, continues when it equals 0 (the real part of the equivalent stiffness becomes negative, for detail see Sec. VI.C) and ends when it moves away from 0. The opposite being a passband. In the stopband, the sound does not propagate (lossless case), or slightly (lossy case), inside the metamaterial. In the stopband, the metamaterial is purely (lossless case), or nearly (lossy case), reflective. This yields nearly zero absorption (hard-backed), see Fig. 4(b), and zero transmission (anechoic-backed) (or, basically, infinite sound transmission loss), see Fig. 4(c). For frequencies under the cutoff frequency (30 kHz), three stopbands (2170-10254 Hz, 11762-19063 Hz, and 20721-27808 Hz) are observed, each and linked to a DE resonance.

The phase change in the dispersion curve and the peaks of the peaks of transmission loss in the stopbands are associated to the resonances of the DE, which can be determined by solving numerically $\mathrm{Im}\left(Z_{S,AHR}\right) = 0$, Eq. (9). The DE resonances are responsible of the sudden drop of the acoustic wavenumber, Fig. 4(a). The frequencies of the DE resonances f_{DE} differ slightly from the frequencies corresponding to the beginning of the stopbands. The beginning of a stopband depends on the spacing between DE[32–34]. Because the spacing is small for the studied geometry, the DE resonances are close to the beginning of the stopbands. For the infinite periodic configuration with losses, the beginning of a stopband is deduced from the numerical resolution of Eq. (30), when $\mathrm{Re}(q)h_{cell} = \pi$, i.e. when $f = \mathrm{Re}\left(\frac{1}{\pi}\sqrt{\frac{K_{eq}(f)}{M_{eq}(f)}}\right)$. The zoom in Fig. 4(a) shows that for the lossless case, the start of a stopband beginning clearly at $\mathrm{Re}(q)h_{cell} = \pi$. For the lossy case, the beginning of a stopband appears at a smaller frequency and for a value of $\mathrm{Re}(q)h_{cell}$ less than π. Moreover, the increase in sound transmission loss, Fig. 4(c), starts to increase at a lower frequency than the beginning of a stopband in the lossy case. This is due to two main effects: the finite size of the material and the fact that the end masses are larger due to the end corrections. Anyway, the formula $f = \mathrm{Re}\left(\frac{1}{\pi}\sqrt{\frac{K_{eq}(f)}{M_{eq}(f)}}\right)$ gives a good estimation of the beginning of the stopbands.

B. Modal displacement of masses

The mass-spring model is now used to visualize and analyze the displacements of the masses (i.e., global air displacements of the main pores) in the studied metamaterial for the hard-backed termination. Fig. 5 shows the acoustic displacement mapping of the masses as a function of frequency. The displacement is normalized by the incident displacement. Note that although the mapping is continuous, only displacements at mass positions exist. The masses are at the positions indicated by the horizontal dashed lines, while the vertical solid black lines indicate the beginning and end of a stopband. Fig. 5(a) shows the mapping when losses are considered, while Fig. 5(b) is in the lossless case – both mappings have similarities. As for it, Fig. 5(c) represents a zoom on the first passband and stopband in the lossless case.

In Fig. 5, the vertical lines in yellow are the modal lines. Each corresponds to an eigenfrequency of the metamaterial, the first four eigenfrequencies of which are given in TABLE III. Since the system has N=10 moving masses (hard-backed), 10 modal lines appear in a passband. Similarly, the dark red lines are the nodal lines, where zero displacement occurs. The number of times a modal line is crossed by a nodal line marks the mode number. For example, since only one nodal line (the horizontal one at the rigid termination) intersects the first modal line in the first passband, the first mode is mode 1. Note that the same 10 modes repeat in each passband. This is counter-intuitive compared to a linear mass-spring system or the one-dimensional monatomic chain which will have a finite number of modes equal to the number of degrees-of-freedom. Since a "spring" in the metamaterial has a frequency-dependent stiffness derived from an AHR having multiple natural frequencies, $\mathrm{Im}(Z_{S,AHR} = 0)$, the same 10 modes will repeat in each passband. The modal lines associated with these 10 modes are easier to see in the lossless case since the modal and nodal lines are smeared out in the highest passbands in the lossy case.

In Fig. 5(c), it should be noted that when a nodal line intersects a modal line at an exact mass position (a vertical dashed line), that corresponding mass is stationary and no viscous loss is produced by that mass. On the contrary, when the intersection does not fall exactly at a mass position, that mass will always be in motion and will always produce viscous loss. For example, the tenth mass at 27 mm will always move in the first passband since its position never falls at an intersection of a modal and nodal line. The authors believe that this understanding of the position of masses relative to nodal and modal lines could potentially be useful in optimizing the design of these metamaterials by preventing masses from falling close to a nodal line. For now, such optimization remains to be done and is not the purpose of this article.

Figs. 6 and 7 show the modal shapes, in the lossy case, for the first three modes, and the displacement shape in the first stopband for the hard and anechoic backed terminations, respectively. For the hard-backed termination, Fig. 6, the first three mode shapes in the first passband are another visualization of the first three modal lines of Fig. 5(a) (the vertical lines in yellow). The filled areas in the graphs are the envelopes over a time period at the corresponding frequency. The blue dots represent the 11 masses of the mass-spring representation of the metamaterial at an instant corresponding to a maximum amplitude.

In the hard-backed termination, the last mass is logically always stationary. In Fig. 6, one can recognize that the first mode for the hard-backed termination is the quarter-wave resonance, whereas it is the rigid mode for the anechoic-backed termination. The other mode shapes in the first passband are also those typical of a linear system. Recall that these same mode shapes will repeat in each passband with higher attenuation for higher passbands.

Finally, Figs. 6 and 7 show that in a stopband the mass displacement quickly decreased through the material. In this case, the material is almost reflective, and all the sound is mainly reflected by the first mass-spring cell. The insets in Figs. 6 and 7, for the "In stopband" case, show the acoustic pressure distribution from the first to third mass. One can note that the pressure at the first mass is nearly twice the amplitude of the incident pressure. This represents the blocked pressure on a hard wall having a reflection coefficient of nearly 1. Note that the acoustic pressure was easily obtained here from the displacements calculated by the mass-spring model by solving Euler's equation with a finite difference scheme. See supplementary materials for figures of acoustic pressure profiles and animations of mass displacements for the first modes and in the first stopband for the hard and anechoic backed terminations.

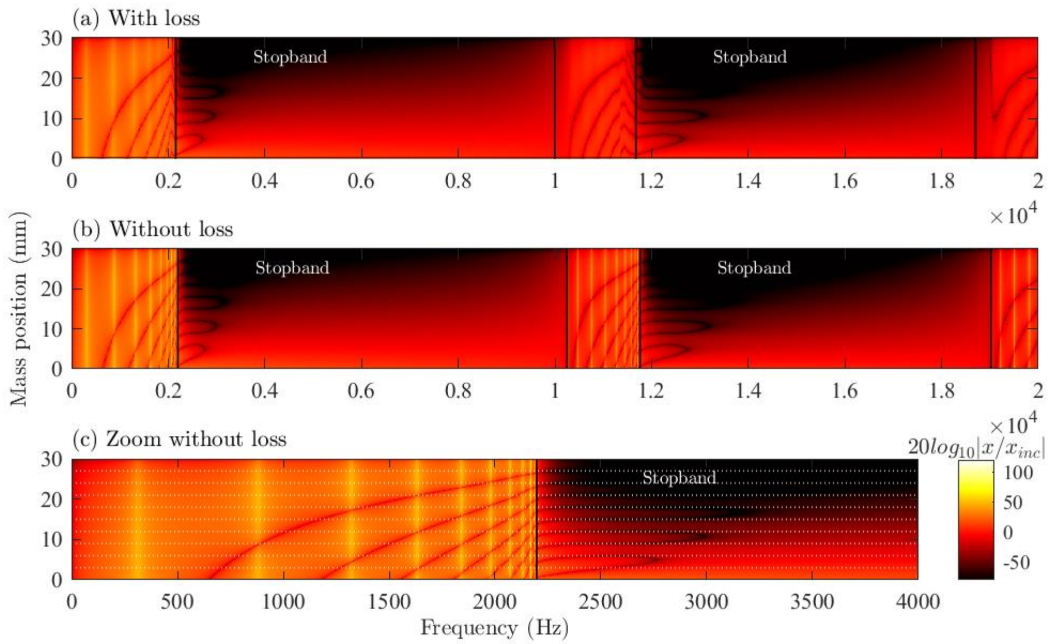

FIG. 5 (Color online). Displacement mapping of the masses as a function of frequency for the hard-backed termination. Cubic interpolation is used to obtain a continuous mapping. The positions of the masses are indicated by the horizontal dashed lines. The beginning and end of the stopbands are indicated by the vertical black lines.

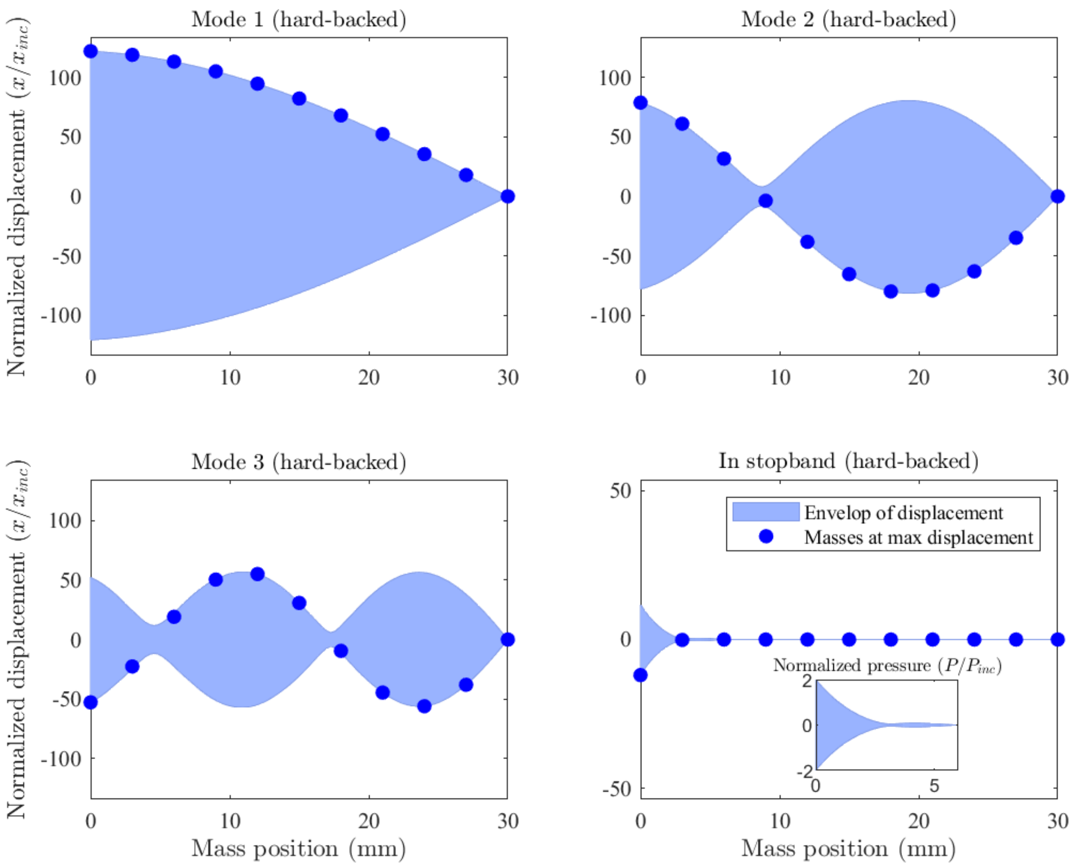

FIG. 6 (Color online). Mass displacement profile with loss at the first modes and in the stopband for the hard-backed termination.

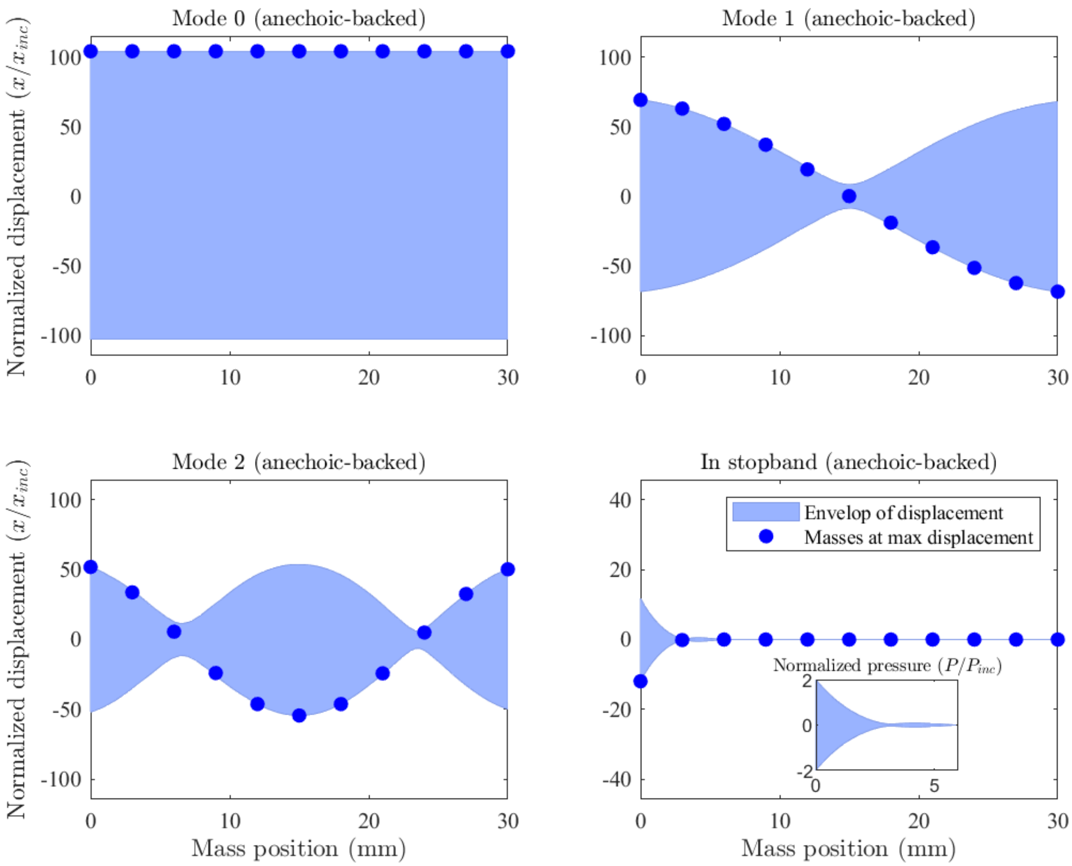

FIG. 7 (Color online). Mass displacement profile with loss at the first modes and in the stopband for the anechoic-backed termination.

C. Analysis of the equivalent stiffness

As discussed earlier, in a conventional infinite periodic one-dimensional monatomic chain, only one stopband band is present. For a frequency greater than the single occurrence $f = \pi^{-1}\sqrt{K/M}$, the disturbance does not propagate. For our metamaterial, the presence of other passbands is due to the fact that it has several stopbands starting at all occurrences $f = \pi^{-1}\sqrt{K_{eq}(f)/M_{eq}(f)}$. This is because the equivalent stiffness is related to the DE resonances via Eq. (21). At a DE resonance the amplitude of the stiffness exhibits a drop, see Fig. 8(b). Its real part is then equal to zero, see Fig. 8(a), then becomes negative before becoming positive again in the next bandwidth. For each bandwidth, a new problem of $N + 1$ degrees-of-freedom (or N in the case of a hard-backed termination) is redefined with a higher equivalent stiffness leading to the same modes at higher frequencies. The values of K_{eq} increase with the order of the passband. Fig. 8(b) shows that the stiffness values nearly double from one passband to the next. The fact that the stiffness and the thermo-viscous losses grow with the frequency explains why the maximum absorption or transmission (transmission loss) decreases (increases) with the order of the passband.

Finally, in the first passband, it can be observed that the amplitude of the stiffness is quasi-static at low frequencies and decreases abruptly as the first resonance DE approaches. This decrease in stiffness when approaching the DE resonance explains why the resonances of the metamaterial (absorption or transmission loss peak) are closer to each other with frequency. Near the DE resonance, they overlap.

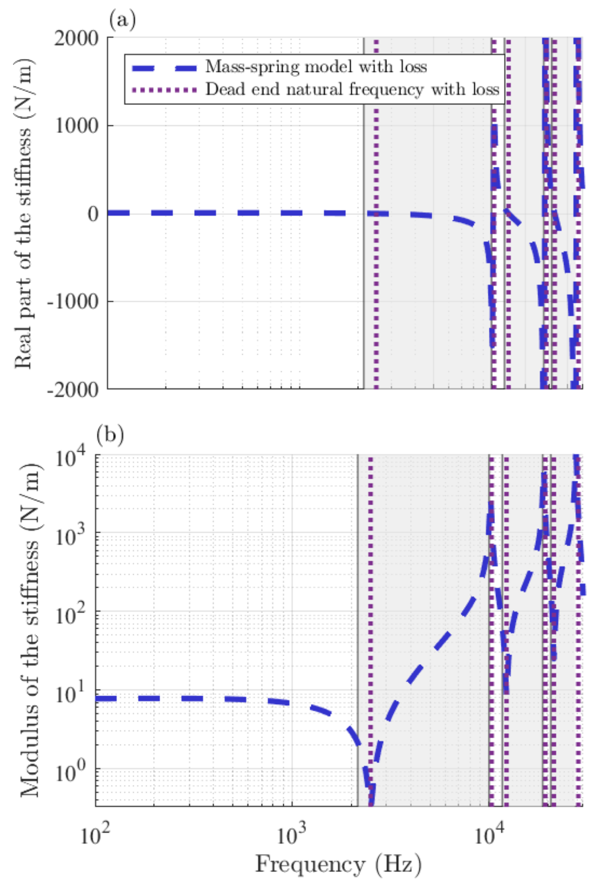

FIG. 8 (Color online). Real part (a) and modulus (b) of the equivalent stiffness as a function of frequency in the lossy case. Stopbands are indicated by grey areas and are delineated by grey lines.

VII. CONCLUSION

A mass-spring model was developed to study metamaterials composed of a compact linear periodic array of thin ring resonators along a main central pore. This resulted in an acoustic equation of motion, where the degrees of freedom are the air motion in each pore segment between the resonators. The resonators were modeled by introducing a surface impedance into the equivalent stiffness matrix of the developed acoustic equation of motion. While the surface impedance can be developed for different types of resonators, this article has developed that of a ring-shaped Helmholtz resonator. From the mass-spring model, a modal analysis of eigenfrequencies and mode shapes was performed, and a formula predicting the first resonance was proposed. The model was used to study the band structure of the metamaterial which shows an infinite succession of passbands and stopbands. In each passband, *N* resonances were observed, where *N* is also the number of masses in the mass-spring model. Unlike a linear mass-spring system of *N* degrees of freedom, the *N*-mass metamaterial exhibits an infinite number of degrees of freedom. An original representation of the band structure in terms of cartography of acoustic displacement of masses as a function of frequency has been proposed. This representation made it possible to better understand the acoustic behavior of the metamaterial in relation with the intersections between the nodal lines, the modal lines and the localization of the masses. To validate the model, a prototype of the metamaterial was machined in aluminum. The prototype was tested in an acoustic tube for normal incidence sound absorption and sound transmission loss. A good correlation between the experimental results and the model predictions was obtained.

ACKNOWLEGEMENTS

The authors acknowledge the financial support of Natural Sciences and Engineering Research Council (NSERC) [funding reference numbers: RGPIN-2018-06113 and RGPIN-2019-06573].

SUPPLEMENTARY MATERIAL

See supplementary material for figures of acoustic pressure profiles inside the material and animations of mass displacements for the first modes and in the first stopband for the hard and anechoic backed terminations.

AUTHOR DECLARATIONS

Conflict of Interest

The authors state that they have no conflict of interests to disclose.

DATA AVAILABILITY

The data that support the findings of this study are available from the corresponding author upon reasonable request.

APPENDIX: IMPEDANCE MATRIX TO TRANSFER MATRIX

The passage of the acoustic impedance matrix to the transfer matrix is here demonstrated. The acoustic impedance matrix is defined as $\mathbf{Z}\boldsymbol{u} = \boldsymbol{p}$, Eq. (24) ($\mathrm{N}+1$ by $\mathrm{N}+1$ matrix). Thereafter, the matrix coefficients of $\mathbf{Z}$ are noted z.

The Cramer's rule gives

$$u_k = \frac{\det(\mathbf{Z}_k)}{\det(\mathbf{Z})}, \tag{A1}$$

where $\mathbf{Z}_k$ is a square matrix formed by replacing the k-th column of $\mathbf{Z}$ by the external pressure acoustic vector $\boldsymbol{p} = \{P_1 \quad 0 \quad \dots \quad 0 \quad -P_{N+1}\}^T$. The input and output acoustic velocities can be deduced with

$$u_1 = \frac{\det(\mathbf{Z}_1)}{\det(\mathbf{Z})}, \tag{A2a}$$

$$u_{N+1} = \frac{\det(\mathbf{Z}_{N+1})}{\det(\mathbf{Z})}, \tag{A2b}$$

where

$$\det(\mathbf{Z}_1) = \begin{vmatrix} P_1 & z_{12} & 0 & \cdots & 0 \\ 0 & z_{22} & & & \vdots \\ \vdots & & \ddots & & 0 \\ 0 & & & \ddots & z_{N,N+1} \\ P_{N+1} & 0 & & z_{N+1,N} & z_{N+1,N+1} \end{vmatrix} = \begin{matrix} P_1 \det(\mathbf{Z}_{2:N+1,2:N+1}) \\ -(-1)^{N+2} P_{N+1} \det(\mathbf{Z}_{1:N,2:N+1}) \end{matrix} \tag{A3}$$

and

$$\det(\mathbf{Z}_{\mathrm{N}+1}) = \begin{vmatrix} z_{11} & z_{12} & & 0 & P_1 \\ z_{21} & \ddots & & & 0 \\ 0 & & \ddots & & \vdots \\ \vdots & & & z_{N,N} & 0 \\ 0 & \cdots & 0 & z_{N+1,N} & P_{N+1} \end{vmatrix} = \begin{matrix} (-1)^{N+2} P_1 \det(\mathbf{Z}_{2:N+1,1:N}) \\ -P_{N+1} \det(\mathbf{Z}_{1:N,1:N}) \end{matrix}. \tag{A4}$$

Combining and rearranging Eq. (A2b) and Eq. (A4) leads to

$$P_1 = \frac{P_{N+1}\det(\mathbf{Z}_{1:N,1:N}) + u_{N+1}\det(\mathbf{Z})}{(-1)^{N+2}\det(\mathbf{Z}_{2:N+1,1:N})}. \tag{A5}$$

Combining Eq. (A2a) and Eq. (A3) leads to

$$u_1 = \frac{P_1\det(\mathbf{Z}_{2:N+1,2:N+1}) - (-1)^{N+2}P_{N+1}\det(\mathbf{Z}_{1:N,2:N+1})}{\det(\mathbf{Z})}. \tag{A6}$$

Replacing P_1 by its expression given by Eq. (A5), u_1 can be rewritten

$$u_1 = \begin{matrix} -P_{N+1}\frac{1}{\det(\mathbf{Z})}\left((-1)^{N+2}\det(\mathbf{Z}_{1:N,2:N+1}) - \frac{\det(\mathbf{Z}_{1:N,1:N})\det(\mathbf{Z}_{2:N+1,2:N+1})}{(-1)^{N+2}\det(\mathbf{Z}_{2:N+1,1:N})}\right) \\ +u_{N+1}\frac{\det(\mathbf{Z}_{2:N+1,2:N+1})}{(-1)^{N+2}\det(\mathbf{Z}_{2:N+1,1:N})} \end{matrix}. \tag{A7}$$

Finally, the transfer matrix is obtained from Eq. (A5) and Eq. (A7)

$$\begin{Bmatrix} P_1 \\ u_1 \end{Bmatrix} = (-1)^{N+1}\begin{bmatrix} \frac{\det(\mathbf{Z}_{1:N,1:N})}{\det(\mathbf{Z}_{2:N+1,1:N})} & \frac{\det(\mathbf{Z})}{\det(\mathbf{Z}_{2:N+1,1:N})} \\ -\frac{\det(\mathbf{Z}_{1:N,2:N+1})}{\det(\mathbf{Z})} + \frac{\det(\mathbf{Z}_{1:N,1:N})\det(\mathbf{Z}_{2:N+1,2:N+1})}{\det(Z)\det(\mathbf{Z}_{2:N+1,1:N})} & \frac{\det(\mathbf{Z}_{2:N+1,2:N+1})}{\det(\mathbf{Z}_{2:N+1,1:N})} \end{bmatrix}\begin{Bmatrix} P_{N+1} \\ u_{N+1} \end{Bmatrix}. \tag{A8}$$

REFERENCES

[1]G. Ma, M. Yang, S. Xiao, Z. Yang, and P. Sheng, "Acoustic metasurface with hybrid resonances," Nat. Mater. **13**, 873–878 (2014).

[2]C. Cai, and C. M. Mak, "Hybrid noise control in a duct using a periodic dual Helmholtz resonator array," Appl. Acoust. **134**, 119–124 (2018).

[3]S. Huang, X. Fang, X. Wang, B. Assouar, Q. Cheng, and Y. Li, "Acoustic perfect absorbers via Helmholtz resonators with embedded apertures," J. Acoust. Soc. Am. **145**, 254–262 (2019).

[4]C. Zhang, and X. Hu, "Three-Dimensional Single-Port Labyrinthine Acoustic Metamaterial: Perfect Absorption with Large Bandwidth and Tunability," Phys. Rev. Appl. **6**, 064025 (2016).

[5]C. R. Liu, J. H. Wu, X. Chen, and F. Ma, "A thin low-frequency broadband metasurface with multi-order sound absorption," J. Phys. D: Appl. Phys. **52**, 105302 (2019).

[6]X. Peng, J. Ji, and Y. Jing, "Composite honeycomb metasurface panel for broadband sound absorption," J. Acoust. Soc. Am. **144**, EL255–EL261 (2018).

[7]P. Leclaire, O. Umnova, T. Dupont, and R. Panneton, "Acoustical properties of air-saturated porous material with periodically distributed dead-end pores," J. Acoust. Soc. Am. **137**, 1772–1782 (2015).

[8]J.-P. Groby, W. Huang, A. Lardeau, and Y. Aurégan, "The use of slow waves to design simple sound absorbing materials," Journal of Applied Physics **117**, 124903 (2015).

[9]J.-P. Groby, R. Pommier, and Y. Aurégan, "Use of slow sound to design perfect and broadband passive sound absorbing materials," J. Acoust. Soc. Am. **139**, 1660–1671 (2016).

[10]N. Jiménez, W. Huang, V. Romero-García, V. Pagneux, and J.-P. Groby, "Ultra-thin metamaterial for perfect and quasi-omnidirectional sound absorption," Appl. Phys. Lett. **109**, 121902 (2016).

[11]N. Jiménez, V. Romero-García, V. Pagneux, and J.-P. Groby, "Quasiperfect absorption by subwavelength acoustic panels in transmission using accumulation of resonances due to slow sound," Phys. Rev. B **95**, 014205 (2017).

[12]T. Dupont, P. Leclaire, R. Panneton, and O. Umnova, "A microstructure material design for low frequency sound absorption," Appl. Acoust. **136**, 86–93 (2018).

[13]D. C. Brooke, O. Umnova, P. Leclaire, and T. Dupont, "Acoustic metamaterial for low frequency sound absorption in linear and nonlinear regimes," J. Sound Vib. **485**, 115585 (2020).

[14]T. C. Kone, M. Lopez, S. Ghinet, T. Dupont, and R. Panneton, "Thermoviscous-acoustic metamaterials to damp acoustic modes in complex shape geometries at low frequencies," J. Acoust. Soc. Am. **150**, 2272–2281 (2021).

[15]R. Al Jahdali, and Y. Wu, "Coupled Resonators for Sound Trapping and Absorption," Sci. Rep. **8**, 13855 (2018).

[16]H. Duan, X. Shen, E. Wang, F. Yang, X. Zhang, and Q. Yin, "Acoustic multi-layer Helmholtz resonance metamaterials with multiple adjustable absorption peaks," Appl. Phys. Lett. **118**, 241904 (2021).

[17]C. Guan, and Z. Jiao, "Modeling and Optimal Design of 3 Degrees of Freedom Helmholtz Resonator in Hydraulic System," Chin. J. Aeronaut. **25**, 776–783 (2012).

[18]M. B. Xu, A. Selamet, and H. Kim, "Dual Helmholtz resonator," Appl. Acoust. **71**, 822–829 (2010).

[19]N. W. Ashcroft, and N. D. Mermin, "Classical Theory of the Harmonic Crystal," in *Solid state physics* (Holt, Rinehart and Winston, New York, 1976) pp. 443–472.

[20]M. Lopez, T. Dupont, and R. Panneton, "A mass-spring analogy for modeling the acoustic behaviour of a metamaterial," Inter-Noise **265**, 6295–6301 (2022).

[21]M. L. Munjal, "Propagation of waves in ducts," in *Acoustics of ducts and mufflers : with application to exhaust and ventilation system design* (John Wiley & Sons, New York, 1987) pp. 1–41.

[22]F. C. Karal, "The Analogous Acoustical Impedance for Discontinuities and Constrictions of Circular Cross Section," J. Acoust. Soc. Am. **25**, 327–334 (1953).

[23]U. Ingard, "On the Theory and Design of Acoustic Resonators," J. Acoust. Soc. Am. **25**, 1037–1061 (1953).

[24]N. S. Dickey, and A. Selamet, "Helmholtz resonators: one-dimensional limit for small cavity length-to-diameter ratios," J. Sound Vib. **195**, 512–517 (1996).

[25]R. Fitzpatrick, "Longitudinal standing waves," in *Oscillations and waves an introduction* (CRC press, Boca Raton (Fla.), 2013) pp. 69–88.

[26]F. W. J. Olver, "Bessel Functions of Integer Order," in *Handbook of Mathematical Functions*, edited by M. Abramowitz and I. A. Stegun (United states department of commerce, Washington, D.C, 1972) p. 360.

[27]"Solving the TVA problem in a geometry with a complex shape, even if it looks like a cylindrical pore or a slit, allows a more accurate evaluation of the thermoviscous losses compared to the assignment of effective air properties calculated by an equivalent fluid model such as the JCA model.,"

[28]"This time, according to the method proposed by Karal21, and the geometry studied, only 1.5 mm is added on the side of the pore connected to the external medium. Indeed, on its other side (inner side), the pore is connected to a pore of the same radius and no length correction is to add.,"

[29]Y. Salissou, R. Panneton, and O. Doutres, "Complement to standard method for measuring normal incidence sound transmission loss with three microphones," J. Acoust. Soc. Am. **131**, EL216-22 (2012).

[30]ASTM E1050-19, *Standard Test Method for Impedance and Absorption of Acoustical Materials Using a Tube, Two Microphones and a Digital Frequency Analysis System*, (American Society for Testing and Materials, West Conshohocken, PA, 2019).

[31]P. A. Deymier, "Discrete One-Dimensional Phononic and Resonant Crystals," in *Acoustic Metamaterials and Phononic Crystals* (Springer Series in Solid-State Sciences, 2013) pp. 13–19.

[32]C. E. Bradley, *Acoustic Bloch Wave Propagation in a Periodic Waveguide*, (Defense Technical Information Center, Fort Belvoir, VA, 1991).

[33]N. Sugimoto, and T. Horioka, "Dispersion characteristics of sound waves in a tunnel with an array of Helmholtz resonators," J. Acoust. Soc. Am. **97**, 1446–1459 (1995).

[34]X. Wang, and C. M. Mak, "Acoustic performance of a duct loaded with identical resonators," J. Acoust. Soc. Am. **131**, EL316–EL322 (2012).